Chen et al. *NPG Asia Materials* (2024) 15:72
https://doi.org/10.1038/s41427-023-00518-4

NPG Asia Materials

ARTICLE Open Access

Role of the structure order in the transport and magnetic properties of high-entropy alloy films

Jia-Wei Chen[1], Shih-Hsun Chen[2,3], Padraic Shafer[4], Wen-Yen Tzeng[5], Yi-Cheng Chen[6], Chih-Wei Luo[7], Wen-Wei Wu[1], Jien-Wei Yeh[3,8] and Ying-Hao Chu[1,8,9]

Abstract

The fabrication and development of high-entropy alloys (HEAs) with exceptional functionalities is a rapidly expanding field with numerous applications. When the role of entropy in HEAs is considered, the extrinsic factors, such as the existence of grains and different phases, need to be separated from the intrinsic configurations of the atomic lattice. Here, we fabricated the $CoCrFeNi_2Al_{0.5}$ HEA/muscovite heterostructures, and some were prepared as epitaxial bilayers and others were prepared as an amorphous system. These two systems are classified into atomic-site disordered (ASD) and structurally disordered (SD) states, respectively, without the extrinsic effects for the determination of the crystal lattice role in high-entropy states. In this study, we determined the role of the structure order in correlation with the structural, electronic, and magnetic properties of HEAs using a combination of energy-dispersive X-ray spectrometry, X-ray diffraction, transmission electron microscopy, magneto-transport, ac magnetometry, and X-ray absorption spectroscopy with magnetic circular dichroism. The ASD state showed fully metallic behavior. In contrast, the SD state showed a metallic behavior with intense magnetic saturation, which was called Kondo-like behavior, under 50 K with a low-temperature coefficient of resistivity of ~64 ppm/°C. The difference between the saturation magnetic moment and the electron relaxation behavior in the ASD and SD states resulted from the existence of the structural order affecting the atomic distance and periodicity to modify the exchange interaction and tune the electron-phonon interaction for scattering. The ferromagnetic behavior contributed by Co, Fe, and Ni atoms was probed by X-ray absorption and magnetic circular dichroism to understand the magnetic interactions in the ASD and SD states.

Introduction

The theoretical basis for a novel class of multi-component alloy stabilized by thermodynamic considerations was established in 1996 and dubbed "high entropy alloys" (HEAs). Designed by the terms "configuration entropy" in thermodynamics, the advocate of HEAs predicted that an alloy fused with equiatomic amounts of transition metal elements would reach the high entropy state and become a single stable phase[1,2]. In 2004, Yeh's group successfully fabricated $CuCoNiCrAl_xFe$ high-entropy alloys[3], a breakthrough that impacted the field of metallurgy and confirmed the feasibility of the theory. After the concept of a high-entropy alloy (HEA) was proposed, the Cantor alloy, CoCrFeMnNi, became the most representative HEA system due to its phase constitution of a single FCC solid solution[4]. This result prompted many high entropy-related studies, and scientists began to design alloys with a wide variety of compositions and conducted in-depth exploration of high entropy effects[5–7]. However, typical HEAs are polycrystalline or have a small portion of a precipitation phase[8–10], and the contribution of the atomic randomness to the study of physical properties is difficult to distinguish. As the development of HEAs becomes established, more research has been performed in this field to investigate more unknown properties. To further study the

Correspondence: Shih-Hsun Chen (brucechen@nycu.edu.tw) or Ying-Hao Chu (yhchu@mx.nthu.edu.tw)
[1]Department of Materials Science and Engineering, National Yang Ming Chiao Tung University, Hsinchu 30010, Taiwan
[2]Department of Mechanical Engineering, National Yang Ming Chiao Tung University, Hsinchu 30010, Taiwan
Full list of author information is available at the end of the article

relationship between the high entropy effect and physical properties, we designed a new state of HEAs through special van der Waals heteroepitaxy[11–13]; to avoid defect creation at the interface due to a lattice mismatch. In the field of magnetism, the cantor alloy has been studied for its unique spin glass transition at low temperatures. In this study, we used another well-established HEA, $CoCrFeNi_2Al_{0.5}$, as a new model to start a novel exploration[14–16]. We fabricated a single-crystal face-centered cubic (FCC) epitaxial high-entropy alloy film and an "alloy metallic glass," which are viewed as being crystalline and noncrystalline, respectively. To better define the difference between the two systems, the "single crystal FCC epitaxial" high entropy alloy film was named an "atomic site disordered" (ASD) state due to the random occupation of constituent elements at each lattice site, corresponding to the original concept of HEA with a substantial contribution from the configuration entropy. The "alloy metallic glass" had no long-range order of its atomic positions and no discernable crystal structure. Defining the contribution of configuration entropy from the lattice is not straightforward in this state. This state was called "structurally disordered" (SD). A series of structural, magnetic, and electric properties were measured to compare their differences and to provide an understanding of the role of the lattice. The chemical uniformity of the element distribution was verified by energy-dispersive X-ray spectrometry mapping. X-ray diffraction and transmission electron microscopy confirmed the epitaxy of the ASD state. The magneto-transport was measured as a function of temperature using a four-point probe. The magnetic response was characterized by magnetic hysteresis measurements, and local electronic and magnetic structures were investigated by X-ray absorption spectroscopy and magnetic circular dichroism. In this study, the role of the lattice and its affect on the physical properties of HEAs were also described.

Materials and methods

Materials

The muscovite substrates were purchased from Taiwan Epitaxial Thin Film Corporation Limited. They were then cut into a suitable size and exfoliated with 3 M double-sided tape to achieve the proper thickness. The thickness of muscovite was detected by a spiral micrometer. DI water and nitrogen gas were used to clean the muscovite surface.

Thin film fabrication

HEA films were prepared on F-mica substrates by DC magnetron sputtering. The sputtering target was a $CoCrFeNi_2Al_{0.5}$ ingot with a diameter of 3" and thickness of 6 mm. The temperature was controlled at 650 °C with an Ar pressure of 3 mTorr to obtain unique ASD samples. The SD samples were deposited at room temperature at the same pressure with Ar gas. The base pressure of the high vacuum chamber was less than 3×10^{-6} Torr to prevent oxidation when the deposition began. The thickness of the samples was controlled to 300 nm to obtain standard information on the physical properties.

Structural identification

Synchrotron-based XRD techniques at beamline 17B in the National Synchrotron Radiation Research Center were used for structural characterization. The cross-sectional TEM specimens were prepared using the focus ion beam technique (Hitachi NX2000). High-resolution TEM images were obtained using a JEOL JEM-F200 microscope.

Magnetic properties

The temperature-dependent magnetization, magnetic hysteresis loop, and temperature-dependent hysteresis loop were obtained using Quantum Design PPMS.

Electrical property

The temperature-dependent resistance, magnetoresistance, and Hall measurements were performed using Quantum Design PPMS. The sample was mounted on the standard PPMS puck. The longitudinal resistance was measured by a four-probe method, and the Hall measurement was conducted with the classic Hall-bar geometry.

X-ray absorption & X-ray magnetic circular dichroism

XAS and XMCD were performed at beamline 4.0.2 of the Advanced Light Source. The data were collected at 50 K in total electron yield mode and luminescence yield. The sample was aligned with the applied magnetic field and X-ray propagation direction in grazing incidence with the beam and field inclined at 20° relative to the film plane. The hysteresis signal of each element was collected with a particular circular polarization and scanned with the hysteresis field. Therefore, all measurements were performed using alternating photon helicity with ±0.9 circular polarization.

Ultrafast dynamics spectroscopy

Ultrafast dynamics spectroscopy was performed using a degenerate pump-probe system (light source: repetition rate: 5.2 MHz, wavelength: 800 nm, pulse duration: 100 fs) with an avalanche photodetector and the standard lock-in technique. The fluences of the pump and probe beams were 96 and 8 $\mu J/cm^2$, respectively. The corresponding photon energy of the pump pulses was 1.55 eV for 800 nm. The photoexcited electron dynamics were examined by measuring the photoinduced transient reflectivity changes ($\Delta R/R$) of the probe beam with a

photon energy of 1.55 eV (800 nm). At zero-time delay, the number of photoexcited electrons generated by the nonthermal process was related to the amplitude of $\Delta R/R$. These high-energy photoexcited electrons in the excited states further released their energy with a time constant of several hundred ps through electron-phonon coupling.

Results

A schematic of the ASD state is shown in Fig. 1a. To demonstrate the randomness of the elements, the circular atom was divided into five colors: Co, Cr, Fe, Ni, and Al. Each colorful atom was arranged at the site of the FCC structure to show the structural ordering. Details on the sample fabrication could be found in "Methods". High-resolution X-ray diffraction was used to characterize the film orientation and quality. Only one peak was detected along with those from the (00L) series of muscovite (Fig. 1b) with no other crystalline phase, and no evident signal was observed in the SD state. According to Bragg's law, the d-spacing of the peak was 2.06 Å. Furthermore, a phi scan was carried out to extract the in-plane information of the HEA/muscovite, as shown in Fig. 1c. Muscovite {202} was detected every 120° and showed threefold symmetry. The signal of the HEA film appeared every 60°, and the presence of the six peaks in the phi scan of the HEA film indicated the existence of two sets of structural domains in the alloy layer. These XRD results confirmed that the HEA film possessed an FCC (111) orientation along the muscovite [00L] direction, and the lattice constant a was 3.568 Å. This value is close to that of FCC Ni, where the atomic proportion could be adjusted. Using a slight swinging ω angle to scan the heterostructure, the rocking curve measurement could provide critical information on crystal quality. The result showed a full width at half maximum (FWHM) of 1.08° for the HEA (111) peak (Fig. 1d). The XRD reciprocal space mapping confirmed the heteroepitaxy and detailed information on the lattice parameters of the HEA film (Fig. 1e). The lattice parameter calculated from the in-plane direction was 3.57 Å, while the parameter was the same as the normal direction; this result indicated FCC stacking of the HEA film. From the RSM and L-scan results in XRD, the strain value was calculated to be 0.05%, and the stress value was estimated to be ~7.5 MPa with an elastic modulus of 150 GPa[17]. The weak stress confirmed that the interaction between the film and substrates was different from conventional epitaxial growth in van der Waals heteroepitaxy. Figure 1f provides information on the interface of the HEA/muscovite heterostructure characterized by high-resolution transmission electron microscopy (HR-TEM). Calibrated fast Fourier transform patterns are shown on the right-hand side of Fig. 1f. In these figures, no dislocations or stacking faults were observed at the interface. We did also not observe the

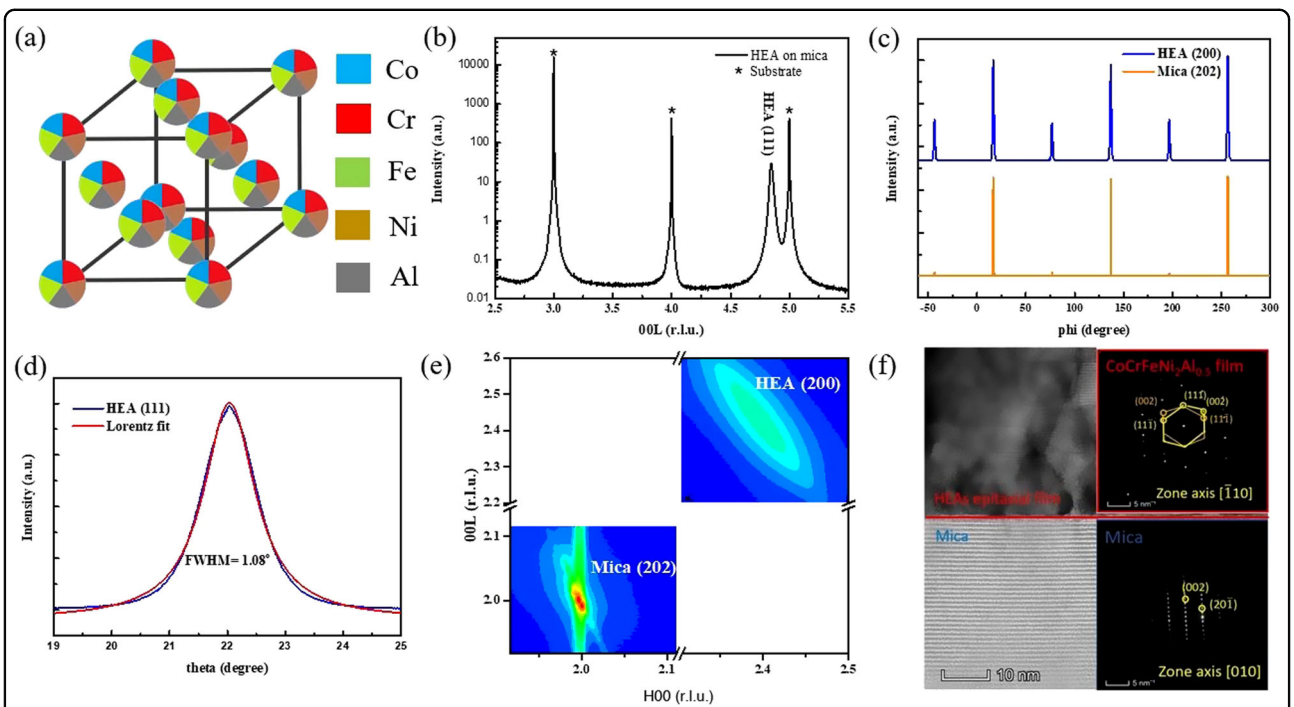

Fig. 1 Structural characteristics of the ASD state. a Schematic of the atomic disorder of the HEA. **b** XRD L-scan along the muscovite (00L) orientation. **c** Rocking curve of HEA (111). **d** ϕ-scan of muscovite (202) and HEA (200). **d** Schematic of the relationship of the metal-muscovite heteroepitaxy. **e** Reciprocal space mapping of muscovite (202) and HEA (200). **f** Cross-sectional HR-TEM of the interface and the related FFT patterns.

sacrificial layer, a thin layer with amorphous or complex oxide forming at the interface. The clear diffraction patterns of HEA and muscovite confirmed the crystal structure and the relationship of the heteroepitaxy and were consistent with the XRD results. The SD samples were deposited using the same growth parameters at room temperature to prevent crystallization.

After establishing the structural information, the structure order of the magnetic properties of the ASD and SD states was examined. To exclude the effect of the composition on magnetic properties, the EDS statistical results of the SD and ASD states from ten spectra were measured to describe the film composition approaching the target (Figure S2, Tables S1 and S2 for the SD state. Figure S3, Tables S3 and S4 for the ASD state). The deviations of these five elements were not over 2% in both states; thus, we could explore the magnetic properties with the structure order. Figure 2a, b shows the typical magnetic hysteresis loops at 50 K for these states. First, the magnetization saturation of the SD state had a value of 330 emu/cm^3; this value was two times larger than that of the ASD state. The saturation of both systems showed shape anisotropy dominant behavior, even if the rotating axis in the ASD state was checked. This typical phenomenon in thin film systems was attributed to the significant difference in scale between the in-plane and out-of-plane directions[18,19]. The magnified image at the low field range of the hysteresis loop at 50 K is shown in Fig. 2c. The coercive field was more significant in the SD state and typically associated with higher saturation and magnetic domain formation[20]. In Fig. 2d, the field-cooled M–T curve was measured with a field of 100 Oe from 400 K to 10 K. Extracted from the first ordered deviation method, the Curie temperature of the ASD state was determined to be 207 K; this result was consistent with Figure S4a. A significant decrease in the saturation moment over 200 K was observed. For the SD state, the magnetization was not diminished in the temperature range, providing good stability of the ferromagnetism. The data shown in Figure S4b also confirmed this result. To understand the mechanism, a molecular field expression[21,22] for the Curie temperature was used, as shown in Eq. (1).

$$T_C = 2J(r)Z_T S(S+1)/3k_B \quad (1)$$

$J(r)$: the distance-dependent interatomic interaction integral; Z_T: the coordination number of transition metal; S: the atomic spin quantum number; k_B: the Boltzmann constant.

The atomic distance is an essential variable for the determination of the magnetic interactions in alloy systems. However, the distance between each element is difficult to distinguish. Figure S5 shows the probable distinguishable difference in the atomic distance distribution. For the ASD state, the atomic distance was more evenly distributed, and the FCC structure caused a

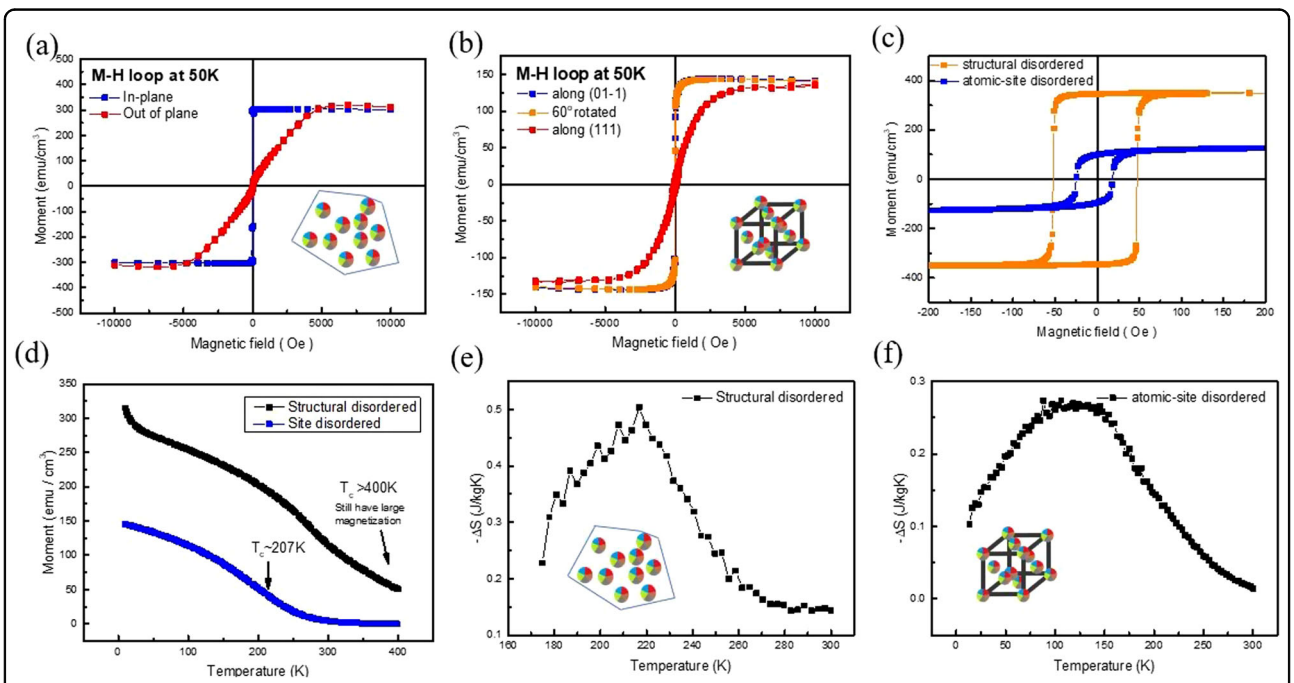

Fig. 2 Magnetic properties of these two states. Magnetic hysteresis loops of the **a** SD and **b** ASD states. **c** Magnified image at the low field. **d** Field cooling M–T curve for these two states. **e** Magnetocaloric effect in the **e** SD and **f** ASD states.

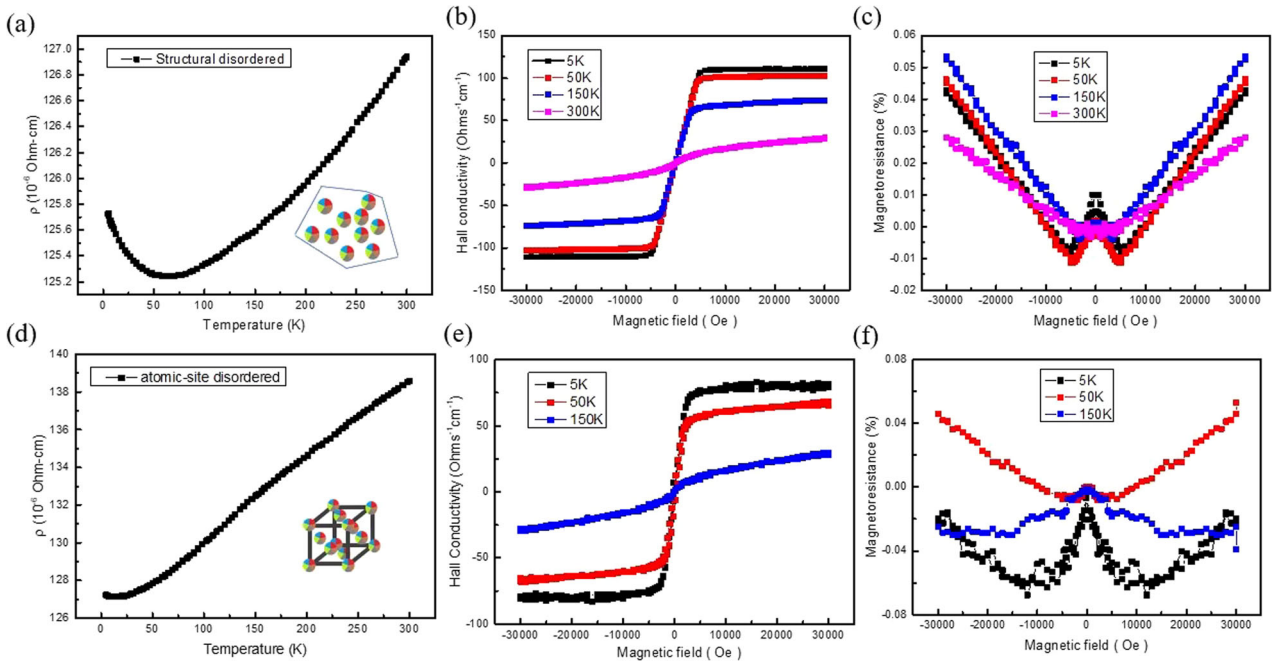

Fig. 3 Electrical and magneto-transport properties of these two states. The resistance-temperature curves of the **a** SD and **d** ASD states. The anomalous Hall effect of the **b** SD and **e** ASD states at different temperatures. The magnetoresistance at various temperatures of the **c** SD and **f** ASD states.

decrease in the ferromagnetic interaction with a fixed atomic distance[23]. The diffraction ring of the SD state is commonly caused by amorphous systems and transformed with FFT, as shown in Figure S6. The distance between the direct beam and the first ring was calculated to be 4.687 nm^{-1}; this value was more significant than 4.473 nm^{-1} for the epitaxial systems. Our results could be used to explain why the atom distance was closer in the SD state, and the broadened ring was related to the broader distance distribution. The atomic distance was distributed more randomly or widely for the SD state. The exchange interaction was greatly dependent on the distance between atoms. Thus, a broader distribution in the SD state created a distinct possibility with short atomic distances, dominating the magnetic behavior. No clear magnetic transition of the SD state was observed due to the distribution of the magnetic interactions resulting from the different distances and elements. When the lattice existed in the ASD state, the distance was fixed, and compared to the SD state, a sharper transition was shown; this result indicated the critical role of the structure order in the HEA. Considering the magnetic entropy effect in these two systems, the calculations of the magnetocaloric effect are shown in Fig. 2e, f. No sharp transition was observed in these two states, exhibiting the randomness outcome. In the SD state, the magnetic entropy change ΔS_m of 0.504 J/kg. K with an applied field of 2 Tesla was measured and provided more significant efficiency in the magnetic refrigeration. In the ASD state, the broader range of the minor entropy change could be discussed with regard to the special effect in high entropy materials. Typically, high entropy systems have a slow reaction with the temperature change[24], caused by the behavior that is dominant by the entropy term in thermodynamics; here, the value of temperature change does not affect the free energy, and this more clearly demonstrates the vital role of the structure order.

After extracting the magnetic characteristics of these systems, we further discuss their electron transport behaviors. The temperature-dependent resistivity measurements for the SD and ASD samples were performed from 300 K to 2 K, as shown in Fig. 3a, d. The ASD state showed metallic behavior and reached a residual resistance approaching 30 K. The resistivity of the SD sample showed metallic behavior from 300 K to 50 K, and the abnormal increase in resistivity at low temperatures was caused by the Kondo-like effect, showing extra scattering by the impurity magnetic elements. In the HEA system, the difference of the impurity versus the matrix is not readily apparent. Here, a special Kondo-like behavior[25] was shown at temperatures below 50 K in the SD state, indicating magnetic element scattering of electrons in this range. The results could be associated with the M–T curve in Fig. 2d, in which the SD state had a remarkable elevation of the magnetization below 30 K. To understand the electrical properties, the electron scattering

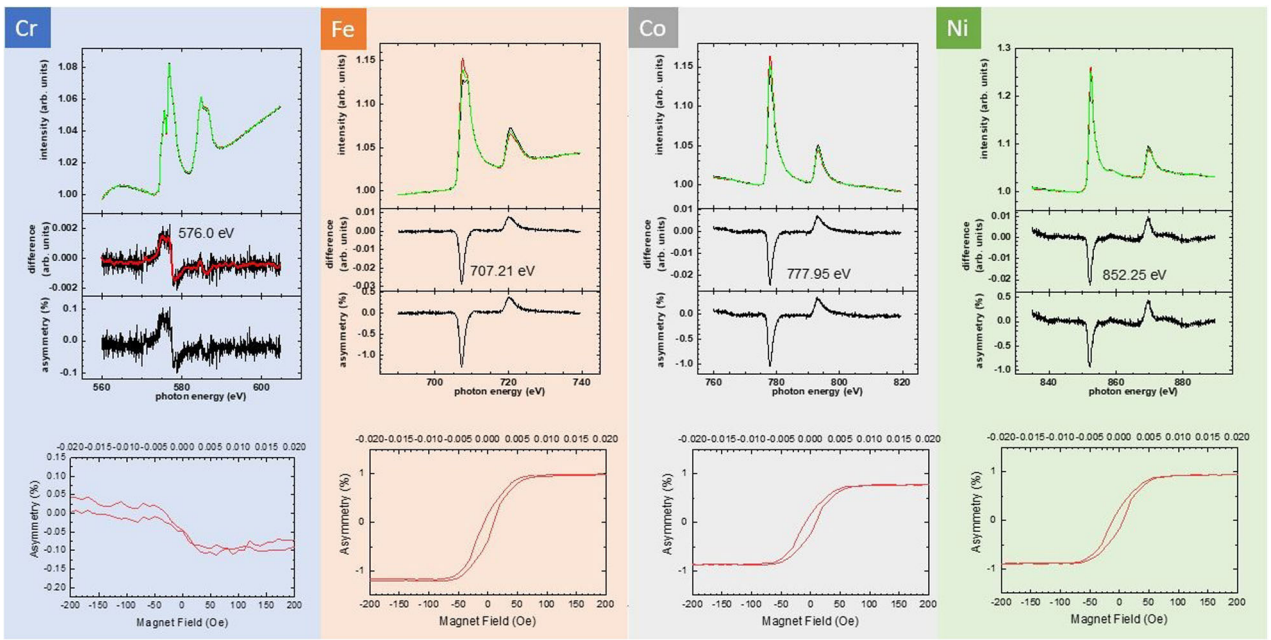

Fig. 4 XAS and XMCD for each magnetic element in the SD state. The hysteresis results of each element are shown in the bottom panel.

mechanism is important. Ultrafast dynamics spectroscopy was used to explore the pathway of electrons[26,27]. In Figure S7a, the shorter relaxation time of 329 ps in the ASD spectrum (478 ps in the SD spectrum) indicated that the energy of the excited electrons in the ASD state was caused by the more efficient phonons. Additionally, as shown in Figure S7b, a pronounced damped oscillation component due to the propagation of a strain pulse[28] further indicated a more ordered lattice structure in the ASD films. These results showed that the FCC lattice could enhance the electron-phonon interaction and were consistent with the resistivity performance at room temperature. To further determine the different electron and spin interactions in these two states, the anomalous Hall effect is shown in Fig. 3b, e. The anomalous Hall conductivity (AHC) linearly increased with the field and changes the slope at the high field (B > 5000 Oe). The slope change was attributed to the saturation of the intrinsic magnetic moment in ferromagnetic thin films. The larger saturation moment in the SD state produced a larger AHC. The reduction in the AHC at higher temperatures confirmed that these phenomena highly correlate with the intrinsic magnetic property[29,30]. The longitudinal magnetoresistance for these two systems is shown in Fig. 3c, f. We measured magnetoresistance at different temperatures to determine whether the high-entropy system would create additional scattering. However, we found that the contribution of the magnetoresistance originated from the magnetization in the films. In Fig. 3c, the "W" type line patterns were related to the magnetic hysteresis loop, in which the width of the "W" was associated with the magnetic coercive field. In Fig. 3f, the different line patterns showed a weak reaction consistent with the weak magnetization in the ASD state. These two states had special positive magnetoresistance, indicating that the Coulomb interaction with spin splitting dominated the magneto-transport property[31].

The results shown in Figures S8a and S8b were used to calculate the temperature coefficient of resistance (TCR) from the R–T curve. Compared to the single elements in these systems in Table S5, the TCR values of these alloy systems were much lower than those of metals, indicating that the entropy term in a high-entropy system could dominate the TCR. The higher value in the ASD state compared to the one in the SD state verified the critical role of structure order. Compared to the SD state, structure order provided periodic atom sites, caused less randomness in the system, and was a critical parameter to show the slow temperature transition.

Next, we aimed to understand each element's role in these two states regarding magnetic contribution. X-ray absorption spectroscopy and magnetic circular dichroism (XAS-MCD) were simultaneously measured. The results from the SD state shown in Fig. 4 are from the surface sensitive total electron yield (TEY) mode; additionally, the results from the ASD state shown in Figures S9 and S10 are from the TEY mode and bulk sensitive luminescence yield (LY) mode, respectively. Cr, Fe, Co, and Ni *L*-edges showed no splitting of their L_2 peaks in either the SD or ASD samples; thus, in these two states, no oxidation occurred for any of these elements. The

hysteresis of the MCD signals (bottom panels of Figures S9 and S11) of each spectrum could be used to distinguish the interactions between each element's magnetization contribution. For these two states, we observed that the aggregate moments of Fe, Co, and Ni atoms were ferromagnetically aligned with the applied field and thus provided the majority of the macroscopically detected magnetization[32]. The Cr signal was too weak to detect in the ASD state; this result was associated with the slight precipitation at the interface between the HEA and muscovite (Figure S12). However, the EDS maps of the SD state are shown in Figure S13, showing the uniform distribution of each element. To exclude the Cr segregation effect on the magnetic property, we measured a series of thickness-dependent MT curves of the ASD state, as shown in Figure S14. The results showed that the magnetic property was not affected in this thickness range, indicating a minor contribution from the Cr segregation at the interface. Then, the film thickness was set to 300 nm; this value was 10 times thicker than the clusters. We expected a strong effect when the film thickness was further reduced. The XMCD results for the luminescence yield and total electron yield were consistent, indicating that the magnetic properties of each element were consistent throughout the thickness of the film. Because the SD state showed no significant qualitative changes in the overall electronic structure or magnetic response of each element, we deduced that the lattice structure did not change the magnetic interactions in these two systems. However, the existence of the structure order could influence the magnitude of macroscopic magnetism, as the SD system exhibited a 200% higher saturation value.

Conclusion

In this study, we fabricated an epitaxial HEA film via van der Waals epitaxy on muscovite. The novel magnetic and transport properties were detailed and established. By a comprehensive observation of the magnetic property, the SD state could maintain a higher magnetization and affect the electron scattering at low temperatures. The FCC lattice structure reduced the exchange interaction in the ASD state. The basics of magnetism with a distance-dependent integral could be used to explain the more significant saturated magnetization produced in the SD state and the exchange interaction weakened by the FCC lattice. An analysis of the relaxation behavior by ultrafast dynamics spectroscopy aided in the understanding of the lattice-enhanced phonon behavior in this high entropy system. XAS-MCD was used to examine the magnetic contribution of each element; here, the ferromagnetic Fe, Co, and Ni atoms led to magnetism in the alloy, and the antiferromagnetic Cr atom negatively contributed to magnetization. Our study contributes to understanding the role of structure order in the HEA system, which can be easily mistaken for the amorphous state.

Acknowledgements
This work was financially supported by the "High Entropy Materials Center" from the Featured Areas Research Center Program within the framework of the Higher Education Sprout Project by the Ministry of Education (MOE) and the Project NSTC 111-2634-F-007-008 by the National Science and Technology Council (NSTC) in Taiwan. In addition, the Ministry of Science and Technology, Taiwan, (grant nos. MOST 106-2119-M-009-011-MY3, 109-2124-M-009-009,109-2124-M-007-004) also provided funding for this project.

Author details
[1]Department of Materials Science and Engineering, National Yang Ming Chiao Tung University, Hsinchu 30010, Taiwan. [2]Department of Mechanical Engineering, National Yang Ming Chiao Tung University, Hsinchu 30010, Taiwan. [3]High Entropy Materials Center, National Tsing Hua University, Hsinchu 30013, Taiwan. [4]Advanced Light Source, Lawrence Berkeley National Laboratory, Berkeley, CA 94720, USA. [5]Department of Electronic Engineering, National Formosa University, Yunlin 632, Taiwan. [6]Institute of Electronic Engineering, National Tsing Hua University, Hsinchu 30013, Taiwan. [7]Department of Electrophysics, National Yang Ming Chiao Tung University, Hsinchu 30010, Taiwan. [8]Department of Materials Science and Engineering, National Tsing Hua University, Hsinchu 30013, Taiwan. [9]Institute of Physics, Academia Sinica, Taipei 115, Taiwan

Author contributions
J.W. Chen and Y.H. Chu designed the project. J.W. Chen supervised the work at NYCU, fabricated the samples, performed the magnetic and transport measurements, and collected the synchrotron XRD. P. Shafer performed the XAS and XMCD measurements. W.Y. Tseng performed the ultrafast dynamics spectroscopy, and the results were discussed with C.W. Luo. S.H. Chen provided high entropy alloy bulk targets and analyzed the structural analysis. W.W. Wu's group obtained the TEM images, performed the EDS analysis, and analyzed the related data. J.W. Chen wrote the first draft, and J.W. Yeh and Y.H. Chu revised the manuscript. All authors discussed the experimental data and commented on the writing of the manuscript.

Conflict of interest
The authors declare no competing interests.

Supplementary information The online version contains supplementary material available at https://doi.org/10.1038/s41427-023-00518-4.

Received: 13 April 2023 Revised: 5 November 2023 Accepted: 14 November 2023.
Published online: 4 January 2024

References

1. Greer, A. L. Confusion by design. *Nature* **366**, 303–304 (1993).
2. Swalin, R. A. in *Thermodynamics of Solids* 2nd edn, 21 (Wiley, 1991).
3. Tong, C. J. et al. Microstructure characterization of Al_xCoCrCuFeNi high-entropy alloy system with multiprincipal elements. *Metall. Mater. Trans. A: Phys. Metall. Mater. Sci.* **36**, 881–893 (2005).
4. Cantor, B., Chang, I. T. H., Knight, P. & Vincent, A. J. B. Microstructural development in equiatomic multicomponent alloys. *Mater. Sci. Eng. A* **375**, 213–218 (2004).
5. Vaidya, M., Pradeep, K. G., Murty, B. S., Wilde, G. & Divinski, S. V. Bulk tracer diffusion in CoCrFeNi and CoCrFeMnNi high entropy alloys. *Acta Mater.* **146**, 211–224 (2018).
6. Gwalani, B. et al. Tensile yield strength of a single bulk $Al_{0.3}$CoCrFeNi high entropy alloy can be tuned from 160 MPa to 1800 MPa. *Scr. Mater.* **162**, 18–23 (2019).
7. Kim, J. et al. Utilization of high entropy alloy characteristics in Er-Gd-Y-Al-Co high entropy bulk metallic glass. *Acta Mater.* **155**, 350–361 (2018).

8. Feng, X. B. et al. Effects of nanotwins on the mechanical properties of Al_x-CoCrFeNi high entropy alloy thin films. *Scr. Mater.* **139**, 71–76 (2017).
9. Marshal, A. et al. Combinatorial evaluation of phase formation and magnetic properties of FeMnCoCrAl high entropy alloy thin film library. *Sci. Rep.* **9**, 1–11 (2019).
10. Ye, Y. F., Wang, Q., Lu, J., Liu, C. T. & Yang, Y. High-entropy alloy: challenges and prospects. *Mater. Today* **19**, 349–362 (2016).
11. Yen, M., Bitla, Y. & Chu, Y. H. van der Waals heteroepitaxy on muscovite. *Mater. Chem. Phys.* **234**, 185–195 (2019).
12. Jiang, J. et al. Flexible ferroelectric element based on van der Waals heteroepitaxy. *Sci. Adv.* **3**, e1700121 (2017).
13. Shi, Z. Q. et al. Van der Waals heteroepitaxial growth of monolayer Sb in a puckered honeycomb structure. *Adv. Mater.* **31**, 1806130 (2019).
14. George, E. P., Raabe, D. & Robert, O. R. High-entropy alloys. *Nat. Rev. Mater.* **4**, 515–534 (2019).
15. Gludovatz, B. et al. A fracture-resistant high-entropy alloy for cryogenic applications. *Science* **345**, 1153–1158 (2014).
16. Cheng, K. C., Chen, J. H., Stadler, S. & Chen, S. H. Properties of atomized AlCoCrFeNi high-entropy alloy powders and their phase-adjustable coatings prepared via plasma spray process. *Appl. Surf. Sci.* **478**, 478–486 (2019).
17. Lu, T. W. et al. Microstructures and mechanical properties of $CoCrFeNiAl_{0.3}$ high-entropy alloy thin films by pulsed laser deposition. *Appl. Surf. Sci.* **494**, 72–79 (2019).
18. Dubowik, J. Shape Anisotropy of magnetic heterostructures. *Phys. Rev. B.* **54**, 1088 (1996).
19. van der Laan, G. Microscopic origin of magnetocrystalline anisotropy in transition metal thin films. *J. Phys. Condens* **10**, 3239 (1998).
20. Han, L. et al. Ultrastrong and ductile soft magnetic high-entropy alloys via coherent ordered nanoprecipitates. *Adv. Mater.* **33**, 2102139 (2021).
21. Kouvel, J. S. & Fisher, M. E. Detailed magnetic behavior of nickel near its Curie point. *Phys. Rev.* **136**, A1626 (1964).
22. Pajda, M., Kudrnovský, J., Turek, I., Drchal, V. & Bruno, P. Ab initio calculations of exchange interactions, spin-wave stiffness constants, and Curie temperatures of Fe, Co, and Ni. *Phys. Rev. B.* **64**, 174402 (2001).
23. Lee, C. et al. Lattice distortion in a strong and ductile refractory high-entropy alloy. *Acta Mater.* **160**, 158–172 (2018).
24. Daw, M. S. & Chandross, M. Sluggish diffusion in random equimolar FCC alloys. *Phys. Rev. Mater.* **5**, 043603 (2021).
25. Kouwenhoven, L. & Glazman, L. Revival of the Kondo effect. *Phys. World* **14**, 33 (2001).
26. Rethfeld, B., Kaiser, A., Vicanek, M. & Simon, G. Ultrafast dynamics of nonequilibrium electrons in metals under femtosecond laser irradiation. *Phys. Rev. B* **65**, 214303 (2002).
27. Sivan, Y. & Spector, M. Ultrafast dynamics of optically induced heat gratings in metals. *ACS Photonics* **7**, 1271–1279 (2020).
28. Chen, L. Y. et al. Ultrafast photoinduced mechanical strain in epitaxial $BiFeO_3$ thin films. *Appl. Phys. Lett.* **101**, 041902 (2012).
29. Tian, Y., Li, Y. & Jin, X. Proper scaling of the anomalous Hall effect. *Phys. Rev. Lett.* **103**, 087206 (2009).
30. Omori, Y. et al. Relation between spin Hall effect and anomalous Hall effect in 3d ferromagnetic metals. *Phys. Rev. B* **99**, 014403 (2019).
31. Rosenbaum, T. F. et al. Low-temperature magnetoresistance of a disordered metal. *Phys. Rev. Lett.* **47**, 1758 (1981).
32. Cao, B. X., Wang, C., Yang, T. & Liu, C. T. Cocktail effects in understanding the stability and properties of face-centered-cubic high-entropy alloys at ambient and cryogenic temperatures. *Scr. Mater.* **187**, 250–255 (2020).